

Failure Prediction of Unidirectional Composites Undergoing Large Deformations¹

Jacob Aboudi

Faculty of Engineering,
Tel Aviv University,
Ramat Aviv 69978, Israel
e-mail: aboudi@eng.tau.ac.il

Konstantin Y. Volokh

Faculty of Civil Engineering,
Technion-Israel Institute of Technology,
Haifa 32000, Israel
e-mail: cvolokh@technion.ac.il

In previous publications, strain-energy functions with limiters have been introduced for the prediction of onset of failure in monolithic isotropic hyperelastic materials. In the present investigation, such enhanced strain-energy functions whose ability to accumulate energy is limited have been incorporated with a finite strain micromechanical analysis. As a result, macroscopic constitutive equations have been established which are capable to predict the onset of loss of static stability in a hyperelastic phase of composite materials undergoing large deformations. The details of the micromechanical analysis, based on a tangential formulation, for composites with periodic microstructure are presented. The derived micromechanical analysis includes the capability to model a possible imperfect bonding between the composite's constituents and to provide the field distribution in the composite. The micromechanical method is verified by comparison with analytical and finite difference solutions for porous hyperelastic materials that are valid in some special cases. Results are given for a rubberlike matrix characterized by softening hyperelasticity, reinforced by unidirectional nylon fibers. The response of the composite to various types of loadings is presented up to the onset of loss of static stability at a location within the hyperelastic rubber constituent, and initial failure envelopes are shown.

[DOI: 10.1115/1.4030351]

Keywords: energy limiters, failure, softening hyperelasticity, rubber, rubber matrix composite, micromechanics, high-fidelity generalized method of cells

1 Introduction

The prediction of failure of isotropic and standard composite materials undergoing small deformations received due to its practical importance great attention. For isotropic materials, failure characterization by the von Mises, Drucker-Prager, and Coulomb-Mohr, for example, have been employed, whereas for composite materials failure criteria such as the maximum stress and strain, Hill, Tsai-Wu, and Christensen have been established and tested, see a recent monograph by Christensen [1] and the many references cited there. These theories are based on macromechanical considerations according to which the composite is regarded as an elastic anisotropic material with known elastic properties. There are however failure theories based on micromechanical analyses which are based on the fiber and matrix properties as well as their detailed interaction. The strain invariant failure theory [2] is one example of such analyses.

The establishment of constitutive equations that govern the large deformations of composite materials which consist of hyperelastic phases is necessary for the modeling and analysis of their behavior. Flexible composites and certain biological tissues are examples of such finite strain multiphase materials. Tires form an example of layered multiphase flexible composite structures that consist of rubbery matrices and stiff reinforcements made of steel wires or synthetic fibers. The high modulus, low elongation cords carry most of the load, and the low modulus, high elongation rubber matrix preserves the integrity of the composite and transfers the load. The primary objective of this type of composite is to withstand large deformation and fatigue loading while providing high load carrying capacity. Another example is the myocardium which is the middle layer in the heart wall, which

consists of parallel muscle fibers that are organized into sheets, thus forming an orthotropic laminated structure with a transversely isotropic behavior in each lamina [3]. In Aboudi et al. [4], an entire chapter has been devoted to the establishment by micromechanical analyses of macroscopic finite strain constitutive equations that govern the behavior of various types of multiphase composites (elastic, viscoelastic, thermoviscoelastic, and viscoplastic).

The various strain-energy functions that have been developed describe the behavior of isotropic materials subjected to large deformations do not predict failure. Failure prediction of hyperelastic materials such as rubbers has been discussed in a recent review by Volokh [5]. The finite strain-energy functions, from which constitutive equations can be established, increase monotonously as the applied deformation increases. This behavior is not realistic since a real material cannot sustain large amount of strain-energy and deformation without failure. Consequently, in a series of publications, the concept of an energy limiter has been introduced, see Volokh [5], for example, and reference cited there. The energy limiter which limits the amount of energy that can be accumulated during deformation is incorporated with the constitutive relation itself which has been designated for the description of the material response. As a result, an enhanced finite strain constitutive equations are obtained which provide the critical values of the strain-energy at which failure of the material occurs and at which its static stability is lost. In addition, it has been shown that the critical values of the modified strain-energy function form a good indicator of the failure of the material when it is subjected to a combined loading. This has been shown by Volokh [6,7] for two types of rubber and for a biological tissue, respectively. It turns out that this critical value is advantageous over other failure criteria such as the critical stretch, stress, shear stress, or von Mises.

In the present investigation, this approach for the prediction of initial failure of monolithic hyperelastic materials is utilized in the micromechanical analysis of composite materials that are undergoing large deformations. Thus, by employing enhanced

¹To Professor Alan Needleman, keen and always engaging.

Contributed by the Applied Mechanics Division of ASME for publication in the JOURNAL OF APPLIED MECHANICS. Manuscript received August 25, 2014; final manuscript received April 8, 2015; published online June 3, 2015. Assoc. Editor: Vikram Deshpande.

strain-energy functions that include these limiters, the micromechanical analysis would provide the critical energy at which a hyperelastic constituent of the composite would fail. This would also lead to the occurrence of the loss of static stability of the composite itself.

In a series of papers, a finite strain micromechanical analysis, referred to as high-fidelity generalized method of cells (HFGMC), which is based on the homogenization technique of periodic composites has been developed. It has been implemented for the establishment of the constitutive behavior of composites which consist various types of hyperelastic and inelastic constituents, see Aboudi et al. [4] and references cited there. The reliability and accuracy of the prediction were extensively examined and verified by Aboudi and Pindera [8] and Aboudi [9] by comparisons with exact, finite element, and finite difference solutions. In the framework of HFGMC method, the periodicity of the composite assumption enables the identification and the analysis of a repeating unit cell which is divided into several subcells. The strain-energy variations of each subcell that is filled with a hyperelastic material are monitored. The first subcell whose strain-energy reaches the critical value determines the initial failure occurrence of the composite caused by the loss of stability of its hyperelastic material at that location.

The present article is organized as follows. Section 2 introduces the necessary modifications of a given strain-energy function that are needed to incorporate the limiters. This is followed by the derivation of the tangential formulation of the resulting constitutive equations of the hyperelastic material. Section 3 presents the finite strain HFGMC incremental micromechanical method, in conjunction with a possible imperfect bonding between the composite constituents. Section 4 presents verifications of the proposed approach by comparisons of the predicted response by the HFGMC analysis of porous materials to biaxial loading with exact and finite difference solutions which are applicable in some special cases. Section 5 presents applications of the softening hyperelasticity on a rubberlike matrix composite reinforced by unidirectional nylon fibers. Conclusions and possible future research are discussed in Sec. 6.

2 Failure Modeling by Softening Hyperelasticity

2.1 Constitutive Equations. Let W denote the strain-energy per unit volume function of isotropic hyperelastic materials. This function can be expressed, in the framework of the Ogden's representation [10,11] in terms of the principal stretches: $\lambda_1, \lambda_2, \lambda_3$. With \mathbf{F} denoting the deformation gradient and \mathbf{F}^T is its transpose, the right $\mathbf{C} = \mathbf{F}^T \mathbf{F}$ Cauchy–Green strain tensor is given in terms of its eigenvalues by the spectral decomposition by

$$\mathbf{C} = \sum_{A=1}^3 \lambda_A^2 \mathbf{N}_A \otimes \mathbf{N}_A, \quad A = 1, 2, 3 \quad (1)$$

where \mathbf{N}_A are the principal referential orthonormal directions.

In the principal coordinates in which \mathbf{C} is given by Eq. (1), the second Piola–Kirchhoff stress tensor \mathbf{S} of the material is determined from

$$S_A = \frac{1}{\lambda_A} \frac{\partial W}{\partial \lambda_A}, \quad A = 1, 2, 3 \quad (2)$$

As the applied deformation on the material increases, both the strain-energy W and the corresponding stress \mathbf{S} increase as well. Theoretically, there are not limits to the increase of these quantities which obviously is not realistic. In order to limit the capacity of the material to accumulate strain-energy during deformation, Volokh [6] introduced the concept of energy limiter. According to this concept, the strain-energy W is replaced by the new strain-energy function ψ .

$$\psi = \psi^F - \psi^E(\mathbf{C}) \quad (3)$$

where ψ^F and $\psi^E(\mathbf{C})$ denote the failure and elastic energies, respectively. The failure energy (energy of full separation) is given by

$$\psi^F = \frac{\phi}{m} \Gamma\left(\frac{1}{m}, 0\right) \quad (4)$$

The elastic energy is defined by

$$\psi^E(\mathbf{C}) = \frac{\phi}{m} \Gamma\left(\frac{1}{m}, \frac{W^m}{\phi^m}\right) \quad (5)$$

where $\Gamma(s, x)$ is the upper incomplete gamma function defined by

$$\Gamma(s, x) = \int_x^\infty t^{s-1} \exp(-t) dt \quad (6)$$

with ϕ and m being material parameters. The constant ϕ represents the energy limiter that describes the limiting value of the accumulated energy of the material whereas the parameter m controls the sharpness of the transition to material instability. Large values of m correspond to steep failure. Gradual transition is typical of some soft biological tissues, whereas rubbers exhibit abrupt transition. The following properties exist:

$$\psi^F = \psi^E(\mathbf{I}); \quad \psi^E(\mathbf{C}) \rightarrow 0, \quad \text{when } \|\mathbf{C}\| \rightarrow \infty \quad (7)$$

where \mathbf{I} is the second-order unit tensor.

The second Piola–Kirchhoff stress tensor can be determined from ψ according to

$$S_A = \frac{1}{\lambda_A} \frac{\partial \psi}{\partial \lambda_A} = \frac{1}{\lambda_A} \frac{\partial W}{\partial \lambda_A} \exp\left(-\frac{W^m}{\phi^m}\right), \quad A = 1, 2, 3 \quad (8)$$

In Fig. 1(a), the strain-energy ψ and first Piola–Kirchhoff $T_1 = \lambda_1 S_1$ are schematically shown against the λ_1 in a uniaxial tension test in the one-direction. It can be observed that as the applied stretch increases, the value of ψ reaches the failure energy limit ψ^F . The resulting stress increases from zero to a maximum value after which it decreases to zero. The corresponding critical value of the energy ψ at which the stress reaches this maximum, is denoted by ψ^c . When $\psi = \psi^c$, the static stability of the material is lost indicating the onset of failure.

The above formulation results in a reversible failure, namely, as the applied deformation after failure decreases the failed material unloads along the same loading path thus exhibiting healing. In order to prevent this unrealistic behavior, Volokh [12] modified the above equations as follows. Equation (3) is replaced by

$$\psi = \psi^F - H(\alpha) \psi^E(\mathbf{C}) \quad (9)$$

where α is a function whose evolution equation is given by

$$\dot{\alpha} = -H\left(\epsilon - \frac{\psi^E}{\psi^F}\right), \quad \alpha(t=0) = 0 \quad (10)$$

and $H(x)$ is the Heaviside step function being equal to zero for $x \leq 0$, and equal to one otherwise. In Eq. (10), ϵ is a small dimensionless parameter.

The resulting second Piola–Kirchhoff stress components, derived from Eq. (9), take the form

$$S_A = \frac{1}{\lambda_A} \frac{\partial \psi}{\partial \lambda_A} = -H(\alpha) \frac{1}{\lambda_A} \frac{\partial \psi^E}{\partial \lambda_A} = \frac{1}{\lambda_A} H(\alpha) \frac{\partial W}{\partial \lambda_A} \exp\left(-\frac{W^m}{\phi^m}\right), \quad A = 1, 2, 3 \quad (11)$$

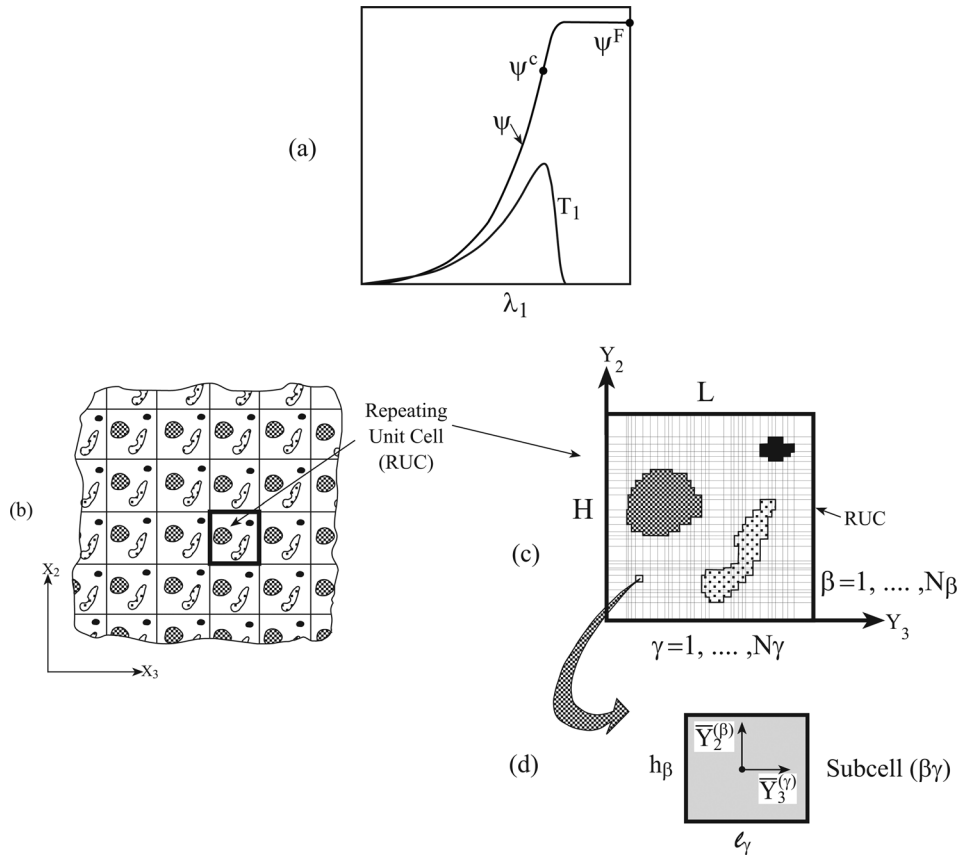


Fig. 1 (a) A schematic representation of the stress T_1 and strain-energy ψ variation of a hyperelastic material with energy limiter. (b) A multiphase composite with doubly periodic microstructures defined with respect to global initial coordinates in the plane X_2 – X_3 . (c) The repeating unit cell is defined with respect to local initial coordinates in the plane Y_2 – Y_3 . (d) A characteristic subcell ($\beta\gamma$) in which a local initial system of coordinates ($Y_2^{(\beta)}, Y_3^{(\gamma)}$) is introduced the origin of which is located at the center.

It can be verified that Eqs. (9)–(11) yield irreversible failure description of the material when the failure energy ψ^F is reached. After reaching its maximum, the stress drops rapidly to zero, where it remains equal to zero upon unloading so that no healing takes place.

2.2 The Tangential Formulation of the Constitutive Equations. The finite strain micromechanical analysis that will be presented in Sec. 3 is based on an incremental procedure which requires the establishment of the instantaneous tangent tensor at any stage of loading. It is also based on the use of the first Piola–Kirchhoff actual stress tensor. To this end, let us express the second Piola–Kirchhoff stress increments which are obtained from Eq. (11) in the form

$$\Delta S_A = H(\alpha) \sum_{B=1}^3 \frac{1}{\lambda_A} \left[\frac{\partial^2 W}{\partial \lambda_A \partial \lambda_B} - \frac{1}{\lambda_A} \frac{\partial W}{\partial \lambda_A} \delta_{AB} - \frac{m}{\phi^m} W^{m-1} \frac{\partial W}{\partial \lambda_A} \frac{\partial W}{\partial \lambda_B} \right] \times \exp\left(-\frac{W^m}{\phi^m}\right) \Delta \lambda_B \quad (12)$$

where δ_{AB} is the Kronecker delta.

The fourth-order symmetric tangent tensor \mathbf{D} in the material description expresses twice the derivative of the second Piola–Kirchhoff stress tensor with respect to the right Cauchy–Green deformation tensor \mathbf{C} , namely

$$\mathbf{D} = 2 \frac{\partial \mathbf{S}}{\partial \mathbf{C}} \quad (13)$$

It can be determined from the following expression [11]:

$$\mathbf{D} = \sum_{A=1}^3 \sum_{B=1}^3 \frac{1}{\lambda_B} \frac{\partial S_A}{\partial \lambda_B} \mathbf{N}_A \otimes \mathbf{N}_A \otimes \mathbf{N}_B \otimes \mathbf{N}_B + \sum_{A=1}^3 \sum_{B \neq A=1}^3 \frac{S_B - S_A}{(\lambda_B)^2 - (\lambda_A)^2} (\mathbf{N}_A \otimes \mathbf{N}_B \otimes \mathbf{N}_A \otimes \mathbf{N}_B + \mathbf{N}_A \otimes \mathbf{N}_B \otimes \mathbf{N}_B \otimes \mathbf{N}_A) \quad (14)$$

Thus far, the above expressions for the stresses, stress increments, and tangent tensors have been referred to the principal directions \mathbf{N}_A . A transformation back to the original coordinates, with respect to which \mathbf{F} is referred to, would provide the corresponding transformed tensors which will be herein denoted, respectively, by \mathbf{S} , $\Delta \mathbf{S}$, and \mathbf{D} . In particular, the following expressions can be written in the original coordinates:

$$\Delta \mathbf{S} = \frac{1}{2} \mathbf{D} : \Delta \mathbf{C} \quad (15)$$

which expresses the increment of the second Piola–Kirchhoff stress tensor in terms of the right Cauchy–Green deformation tensor increment, both of which are referred to the original coordinates (including the fourth-order tangent stiffness tensor \mathbf{D}).

Since the micromechanical analysis uses the actual stresses, let us employ the following relation that provides the first (nonsymmetric) Piola–Kirchhoff stress tensor \mathbf{T} in terms of the second Piola–Kirchhoff stress tensor \mathbf{S} :

$$\mathbf{T} = \mathbf{S} \mathbf{F}^T \quad (16)$$

Consequently, the following incremental constitutive law of the monolithic material is obtained:

$$\Delta \mathbf{T} = \mathbf{R} : \Delta \mathbf{F} \quad (17)$$

where \mathbf{R} is the current first tangent tensor given by

$$R_{ijkl} = D_{irls} F_{jr} F_{ks} + S_{il} \delta_{jk} \quad (18)$$

The incremental constitutive equation (17) of the hyperelastic material with softening will be used in the micromechanical analysis described in the following to determine the macroscopic finite strain behavior of fiber-reinforced composites composed of such constituents.

3 Tangential Formulation of the Finite Strain HFGMC With Imperfect Bonding Between the Phases

The finite strain HFGMC micromechanical method for multiphase materials has been briefly described by Aboudi et al. [4]. In the present article, this method is extended to incorporate the effect of imperfect bonding between the constituents and presented herein in details. This micromechanical analysis is based on the homogenization technique in which a repeating unit cell of the periodic composite is identified. In Fig. 1(b), a multiphase composite with a doubly periodic microstructure defined with respect to the initial global coordinates of the $X_2 - X_3$ plane is shown together with its repeating unit cell, Fig. 1(c), defined with respect to the initial material coordinates $Y_2 - Y_3$. The repeating unit cell is divided into N_β and N_γ subcells in the Y_2 and Y_3 directions, respectively. Each subcell is labeled by the indices $(\beta\gamma)$ with $\beta = 1, \dots, N_\beta$ and $\gamma = 1, \dots, N_\gamma$ and may contain a distinct homogeneous material. The initial dimensions of subcell $(\beta\gamma)$ in the Y_2 and Y_3 directions are denoted by h_β and l_γ , respectively, see Fig. 1(d). A local initial coordinates system $(\bar{Y}_2^{(\beta)}, \bar{Y}_3^{(\gamma)})$ is introduced in each subcell whose origin is located at its center.

In the framework of HFGMC, the increments of the displacement vector $\Delta \mathbf{u}^{(\beta\gamma)}$ in subcell $(\beta\gamma)$ are expanded into second-order polynomials as follows:

$$\begin{aligned} \Delta \mathbf{u}^{(\beta\gamma)} = & \Delta \bar{\mathbf{F}} \cdot \mathbf{X} + \Delta \mathbf{W}_{(00)}^{(\beta\gamma)} + \bar{Y}_2^{(\beta)} \Delta \mathbf{W}_{(10)}^{(\beta\gamma)} + \bar{Y}_3^{(\gamma)} \Delta \mathbf{W}_{(01)}^{(\beta\gamma)} \\ & + \frac{1}{2} \left(3\bar{Y}_2^{(\beta)2} - \frac{h_\beta^2}{4} \right) \Delta \mathbf{W}_{(20)}^{(\beta\gamma)} + \frac{1}{2} \left(3\bar{Y}_3^{(\gamma)2} - \frac{l_\gamma^2}{4} \right) \Delta \mathbf{W}_{(02)}^{(\beta\gamma)} \end{aligned} \quad (19)$$

With $\Delta \bar{\mathbf{F}}$ denoting the increment of the global (macroscopic) deformation gradient, the term $\Delta \bar{\mathbf{F}} \cdot \mathbf{X}$ stands for the increment of the externally applied loading on the composite. The unknown coefficient $\Delta \mathbf{W}_{(mn)}^{(\beta\gamma)}$ is determined, as shown in the following, from the satisfaction of the equilibrium equations, interfacial and periodic conditions.

Expansion (19) yields the deformation gradient increment $\Delta \mathbf{F}^{(\beta\gamma)}$ in subcell $(\beta\gamma)$ which is given by

$$\begin{aligned} \Delta \mathbf{F}^{(\beta\gamma)} = & \Delta \bar{\mathbf{F}} + \begin{bmatrix} 0 & \Delta W_{1(10)}^{(\beta\gamma)} & \Delta W_{1(01)}^{(\beta\gamma)} \\ 0 & \Delta W_{2(10)}^{(\beta\gamma)} & \Delta W_{2(01)}^{(\beta\gamma)} \\ 0 & \Delta W_{3(10)}^{(\beta\gamma)} & \Delta W_{3(01)}^{(\beta\gamma)} \end{bmatrix} \\ & + 3 \begin{bmatrix} 0 & \Delta W_{1(20)}^{(\beta\gamma)} \bar{Y}_2^{(\beta)} & \Delta W_{1(02)}^{(\beta\gamma)} \bar{Y}_3^{(\gamma)} \\ 0 & \Delta W_{2(20)}^{(\beta\gamma)} \bar{Y}_2^{(\beta)} & \Delta W_{2(02)}^{(\beta\gamma)} \bar{Y}_3^{(\gamma)} \\ 0 & \Delta W_{3(20)}^{(\beta\gamma)} \bar{Y}_2^{(\beta)} & \Delta W_{3(02)}^{(\beta\gamma)} \bar{Y}_3^{(\gamma)} \end{bmatrix} \end{aligned} \quad (20)$$

In the absence of body forces, the equilibrium equations in the subcell, expressed in terms of the first Piola–Kirchhoff $\mathbf{T}^{(\beta\gamma)}$ stress tensor, can be represented in the form

$$\frac{\partial T_{2j}^{(\beta\gamma)}}{\partial \bar{Y}_2^{(\beta)}} + \frac{\partial T_{3j}^{(\beta\gamma)}}{\partial \bar{Y}_3^{(\gamma)}} = 0, \quad j = 1, 2, 3 \quad (21)$$

By averaging the increments of the equilibrium equations (21) over the area of the subcell the following relations are obtained:

$$\Delta \mathbf{I}_{2(00)}^{(\beta\gamma)} + \Delta \mathbf{I}_{3(00)}^{(\beta\gamma)} = 0 \quad (22)$$

where $\Delta \mathbf{I}_{2(00)}^{(\beta\gamma)}$ and $\Delta \mathbf{I}_{3(00)}^{(\beta\gamma)}$ can be expressed in terms of the surface-average of the traction increments evaluated along $\bar{Y}_2^{(\beta)} = \pm h_\beta/2$ and $\bar{Y}_3^{(\gamma)} = \pm l_\gamma/2$, respectively. Thus,

$$\begin{aligned} \Delta \mathbf{I}_{2(00)}^{(\beta\gamma)} &= \frac{1}{h_\beta} \left[\Delta \mathbf{T}_2^{+(\beta\gamma)} - \Delta \mathbf{T}_2^{-(\beta\gamma)} \right] \\ \Delta \mathbf{I}_{3(00)}^{(\beta\gamma)} &= \frac{1}{l_\gamma} \left[\Delta \mathbf{T}_3^{+(\beta\gamma)} - \Delta \mathbf{T}_3^{-(\beta\gamma)} \right] \end{aligned} \quad (23)$$

where the surface-average of the traction increments is given by

$$\begin{aligned} \Delta \mathbf{T}_2^{\pm(\beta\gamma)} &= \frac{1}{l_\gamma} \int_{-l_\gamma/2}^{l_\gamma/2} \Delta \mathbf{T}_2^{(\beta\gamma)} \left(\bar{Y}_2^{(\beta)} = \pm \frac{h_\beta}{2} \right) d\bar{Y}_3^{(\gamma)} \\ \Delta \mathbf{T}_3^{\pm(\beta\gamma)} &= \frac{1}{h_\beta} \int_{-h_\beta/2}^{h_\beta/2} \Delta \mathbf{T}_3^{(\beta\gamma)} \left(\bar{Y}_3^{(\gamma)} = \pm \frac{l_\gamma}{2} \right) d\bar{Y}_2^{(\beta)} \end{aligned} \quad (24)$$

and $\Delta \mathbf{T}_2^{(\beta\gamma)}$ and $\Delta \mathbf{T}_3^{(\beta\gamma)}$ are defined by

$$\begin{aligned} \Delta \mathbf{T}_2^{(\beta\gamma)} &= [\Delta T_{21}, \Delta T_{22}, \Delta T_{23}]^{(\beta\gamma)} \\ \Delta \mathbf{T}_3^{(\beta\gamma)} &= [\Delta T_{31}, \Delta T_{32}, \Delta T_{33}]^{(\beta\gamma)} \end{aligned} \quad (25)$$

Substitution of Eq. (23) in Eq. (22) yields

$$\frac{1}{h_\beta} \left[\Delta \mathbf{T}_2^{+(\beta\gamma)} - \Delta \mathbf{T}_2^{-(\beta\gamma)} \right] + \frac{1}{l_\gamma} \left[\Delta \mathbf{T}_3^{+(\beta\gamma)} - \Delta \mathbf{T}_3^{-(\beta\gamma)} \right] = 0 \quad (26)$$

This relation expresses the increments of equilibrium equations imposed in the average sense within subcell $(\beta\gamma)$.

By employing the constitutive relations (17), the following expressions for the components of the surface-average of the traction increments $\Delta \mathbf{T}_2^{\pm(\beta\gamma)}$ and $\Delta \mathbf{T}_3^{\pm(\beta\gamma)}$ are obtained from Eqs. (20) and (24):

$$\begin{aligned} \Delta T_{2j}^{\pm(\beta\gamma)} = & R_{2jkl}^{(\beta\gamma)} \Delta \bar{F}_{kl} + R_{2j12}^{(\beta\gamma)} \left(\Delta W_{1(10)}^{(\beta\gamma)} \pm \frac{3h_\beta}{2} \Delta W_{1(20)}^{(\beta\gamma)} \right) \\ & + R_{2j22}^{(\beta\gamma)} \left(\Delta W_{2(10)}^{(\beta\gamma)} \pm \frac{3h_\beta}{2} \Delta W_{2(20)}^{(\beta\gamma)} \right) \\ & + R_{2j32}^{(\beta\gamma)} \left(\Delta W_{3(10)}^{(\beta\gamma)} \pm \frac{3h_\beta}{2} \Delta W_{3(20)}^{(\beta\gamma)} \right) \\ & + R_{2j13}^{(\beta\gamma)} \Delta W_{1(01)}^{(\beta\gamma)} + R_{2j23}^{(\beta\gamma)} \Delta W_{2(01)}^{(\beta\gamma)} + R_{2j33}^{(\beta\gamma)} \Delta W_{3(01)}^{(\beta\gamma)}, \\ & j, k, l = 1, 2, 3 \end{aligned} \quad (27)$$

$$\begin{aligned} \Delta T_{3j}^{\pm(\beta\gamma)} = & R_{3jkl}^{(\beta\gamma)} \Delta \bar{F}_{kl} + R_{3j12}^{(\beta\gamma)} \Delta W_{1(10)}^{(\beta\gamma)} + R_{3j22}^{(\beta\gamma)} \Delta W_{2(10)}^{(\beta\gamma)} + R_{3j32}^{(\beta\gamma)} \Delta W_{3(10)}^{(\beta\gamma)} \\ & + R_{3j13}^{(\beta\gamma)} \left(\Delta W_{1(01)}^{(\beta\gamma)} \pm \frac{3l_\gamma}{2} \Delta W_{1(02)}^{(\beta\gamma)} \right) \\ & + R_{3j23}^{(\beta\gamma)} \left(\Delta W_{2(01)}^{(\beta\gamma)} \pm \frac{3l_\gamma}{2} \Delta W_{2(02)}^{(\beta\gamma)} \right) \\ & + R_{3j33}^{(\beta\gamma)} \left(\Delta W_{3(01)}^{(\beta\gamma)} \pm \frac{3l_\gamma}{2} \Delta W_{3(02)}^{(\beta\gamma)} \right), \quad j, k, l = 1, 2, 3 \end{aligned} \quad (28)$$

Substitution of Eqs. (27) and (28) in Eq. (26) provides the three relations

$$\begin{aligned} R_{2j12}^{(\beta\gamma)} \Delta W_{1(20)}^{(\beta\gamma)} + R_{2j22}^{(\beta\gamma)} \Delta W_{2(20)}^{(\beta\gamma)} + R_{2j32}^{(\beta\gamma)} \Delta W_{3(20)}^{(\beta\gamma)} \\ + R_{3j13}^{(\beta\gamma)} \Delta W_{1(02)}^{(\beta\gamma)} + R_{3j23}^{(\beta\gamma)} \Delta W_{2(02)}^{(\beta\gamma)} + R_{3j33}^{(\beta\gamma)} \Delta W_{3(02)}^{(\beta\gamma)} = 0, \\ j = 1, 2, 3 \end{aligned} \quad (29)$$

Just like the surface-average traction increments, the surface-average displacements increments can be defined by

$$\begin{aligned} \Delta \mathbf{u}_2^{\pm(\beta\gamma)} &= \frac{1}{l_\gamma} \int_{-l_\gamma/2}^{l_\gamma/2} \Delta \mathbf{u}^{(\beta\gamma)} \left(\bar{Y}_2^{(\beta)} = \pm \frac{h_\beta}{2} \right) d\bar{Y}_3^{(\gamma)} \\ \Delta \mathbf{u}_3^{\pm(\beta\gamma)} &= \frac{1}{h_\beta} \int_{-h_\beta/2}^{h_\beta/2} \Delta \mathbf{u}^{(\beta\gamma)} \left(\bar{Y}_3^{(\gamma)} = \pm \frac{l_\gamma}{2} \right) d\bar{Y}_2^{(\beta)} \end{aligned} \quad (30)$$

In the following, these surface-average increments $\Delta \mathbf{u}_i^{\pm(\beta\gamma)}$, $i = 1, 2, 3$, will be related to the microvariables $\Delta \mathbf{W}_{(mn)}^{(\beta\gamma)}$; $(mn) = 0, 1, 2$; in the expansion (19). To this end, by substituting Eq. (19) in Eq. (30), the following relations are obtained:

$$\begin{aligned} \Delta \mathbf{u}_2^{\pm(\beta\gamma)} &= \Delta \mathbf{W}_{(00)}^{(\beta\gamma)} \pm \frac{h_\beta}{2} \Delta \mathbf{W}_{(10)}^{(\beta\gamma)} + \frac{h_\beta^2}{4} \Delta \mathbf{W}_{(20)}^{(\beta\gamma)} \\ \Delta \mathbf{u}_3^{\pm(\beta\gamma)} &= \Delta \mathbf{W}_{(00)}^{(\beta\gamma)} \pm \frac{l_\gamma}{2} \Delta \mathbf{W}_{(01)}^{(\beta\gamma)} + \frac{l_\gamma^2}{4} \Delta \mathbf{W}_{(02)}^{(\beta\gamma)} \end{aligned} \quad (31)$$

Manipulations of Eq. (31) by subtractions and additions yield

$$\begin{aligned} \Delta \mathbf{W}_{(10)}^{(\beta\gamma)} &= \frac{1}{h_\beta} [\Delta \mathbf{u}_2^+ - \Delta \mathbf{u}_2^-]^{(\beta\gamma)} \\ \Delta \mathbf{W}_{(01)}^{(\beta\gamma)} &= \frac{1}{l_\gamma} [\Delta \mathbf{u}_3^+ - \Delta \mathbf{u}_3^-]^{(\beta\gamma)} \end{aligned} \quad (32)$$

and

$$\begin{aligned} \Delta \mathbf{W}_{(20)}^{(\beta\gamma)} &= \frac{2}{h_\beta^2} [\Delta \mathbf{u}_2^+ + \Delta \mathbf{u}_2^-]^{(\beta\gamma)} - \frac{4}{h_\beta^2} \Delta \mathbf{W}_{(00)}^{(\beta\gamma)} \\ \Delta \mathbf{W}_{(02)}^{(\beta\gamma)} &= \frac{2}{l_\gamma^2} [\Delta \mathbf{u}_3^+ + \Delta \mathbf{u}_3^-]^{(\beta\gamma)} - \frac{4}{l_\gamma^2} \Delta \mathbf{W}_{(00)}^{(\beta\gamma)} \end{aligned} \quad (33)$$

The expressions of $\Delta \mathbf{W}_{(00)}^{(\beta\gamma)}$ in terms of the surface-average displacements increments $\Delta \mathbf{u}_2^{\pm(\beta\gamma)}$ and $\Delta \mathbf{u}_3^{\pm(\beta\gamma)}$ can be achieved by substituting Eq. (33) in Eq. (29). This yields a system of three linear algebraic equations in the three unknowns $\Delta \mathbf{W}_{(00)}^{(\beta\gamma)}$ whose solution expresses these microvariables in terms of $\Delta \mathbf{u}_2^{\pm(\beta\gamma)}$ and $\Delta \mathbf{u}_3^{\pm(\beta\gamma)}$. Hence, this solution together with Eqs. (32) and (33) form the desired expressions which can be formally written as follows:

$$\begin{Bmatrix} \Delta \mathbf{W}_{(00)} \\ \Delta \mathbf{W}_{(10)} \\ \Delta \mathbf{W}_{(01)} \\ \Delta \mathbf{W}_{(20)} \\ \Delta \mathbf{W}_{(02)} \end{Bmatrix}^{(\beta\gamma)} = [\mathbf{S}]^{(\beta\gamma)} \begin{Bmatrix} \Delta \mathbf{u}_2^+ \\ \Delta \mathbf{u}_3^+ \end{Bmatrix}^{(\beta\gamma)} \quad (34)$$

where $\mathbf{S}^{(\beta\gamma)}$ are coefficient matrices whose elements are lengthy and therefore are not given.

Consequently with expressions (34), the following relations can be established from Eqs. (27) and (28):

$$\begin{Bmatrix} \Delta \mathbf{T}_2^\pm \\ \Delta \mathbf{T}_3^\pm \end{Bmatrix}^{(\beta\gamma)} = [\mathbf{K}]^{(\beta\gamma)} \begin{Bmatrix} \Delta \mathbf{u}_2^\pm \\ \Delta \mathbf{u}_3^\pm \end{Bmatrix}^{(\beta\gamma)} + \begin{Bmatrix} \Delta \mathbf{V}_2^\pm \\ \Delta \mathbf{V}_3^\pm \end{Bmatrix}^{(\beta\gamma)} \quad (35)$$

In these equations, the far-field contributions are included in the vectors $\Delta \mathbf{V}_2^{\pm(\beta\gamma)}$ and $\Delta \mathbf{V}_3^{\pm(\beta\gamma)}$ whose components are defined by

$$\begin{aligned} \Delta V_{2j}^{\pm(\beta\gamma)} &= R_{2jkl}^{(\beta\gamma)} \Delta \bar{F}_{kl} \\ \Delta V_{3j}^{\pm(\beta\gamma)} &= R_{3jkl}^{(\beta\gamma)} \Delta \bar{F}_{kl}, \quad j, k, l = 1, 2, 3 \end{aligned} \quad (36)$$

In Eq. (35), $\mathbf{K}^{(\beta\gamma)}$ is a matrix of the 12th-order whose elements depend on the dimension of the subcell and the instantaneous tangent tensor $\mathbf{R}^{(\beta\gamma)}$ of the material filling this subcell.

The continuity conditions of the surface-average traction increments between neighboring subcells require that

$$\begin{aligned} \Delta \mathbf{T}_2^{+(\beta\gamma)} &= \Delta \mathbf{T}_2^{-(\beta+1\gamma)}, \quad \beta = 1, \dots, N_\beta - 1, \quad \gamma = 1, \dots, N_\gamma \\ \Delta \mathbf{T}_3^{+(\beta\gamma)} &= \Delta \mathbf{T}_3^{-(\beta\gamma+1)}, \quad \beta = 1, \dots, N_\beta, \quad \gamma = 1, \dots, N_\gamma - 1 \end{aligned} \quad (37)$$

These conditions provide $3(N_\beta - 1)N_\gamma + 3N_\beta(N_\gamma - 1)$ equations.

In the present article, imperfect bonding between the constituents is allowed. This effect can be modeled by replacing the requirement that the displacements are continuous at the interface between the phases with condition that the difference between these interfacial displacements is proportional to the traction there. This approach provides perfect bonding and complete separation as two special cases of the general imperfect bonding formulation. Accordingly, the following interfacial conditions can be imposed [4]:

$$\begin{Bmatrix} \Delta u_{21}^{+(\beta\gamma)} - \Delta u_{21}^{-(\beta+1\gamma)} \\ \Delta u_{22}^{+(\beta\gamma)} - \Delta u_{22}^{-(\beta+1\gamma)} \\ \Delta u_{23}^{+(\beta\gamma)} - \Delta u_{23}^{-(\beta+1\gamma)} \end{Bmatrix} = \begin{bmatrix} r_T^{(\beta\gamma)} & 0 & 0 \\ 0 & r_N^{(\beta\gamma)} & 0 \\ 0 & 0 & r_T^{(\beta\gamma)} \end{bmatrix} \begin{Bmatrix} \Delta T_{21}^{+(\beta\gamma)} \\ \Delta T_{22}^{+(\beta\gamma)} \\ \Delta T_{23}^{+(\beta\gamma)} \end{Bmatrix} \quad (38)$$

where $\beta = 1, \dots, N_\beta - 1; \gamma = 1, \dots, N_\gamma$ and

$$\begin{Bmatrix} \Delta u_{31}^{+(\beta\gamma)} - \Delta u_{31}^{-(\beta\gamma+1)} \\ \Delta u_{32}^{+(\beta\gamma)} - \Delta u_{32}^{-(\beta\gamma+1)} \\ \Delta u_{33}^{+(\beta\gamma)} - \Delta u_{33}^{-(\beta\gamma+1)} \end{Bmatrix} = \begin{bmatrix} r_T^{(\beta\gamma)} & 0 & 0 \\ 0 & r_T^{(\beta\gamma)} & 0 \\ 0 & 0 & r_N^{(\beta\gamma)} \end{bmatrix} \begin{Bmatrix} \Delta T_{31}^{+(\beta\gamma)} \\ \Delta T_{32}^{+(\beta\gamma)} \\ \Delta T_{33}^{+(\beta\gamma)} \end{Bmatrix} \quad (39)$$

where $\beta = 1, \dots, N_\beta; \gamma = 1, \dots, N_\gamma - 1$. In these equations, $r_N^{(\beta\gamma)}$ and $r_T^{(\beta\gamma)}$ are two parameters that characterize the degree of imperfect bonding at the phase interface in the normal and tangential directions. The values of $r_N^{(\beta\gamma)} = r_T^{(\beta\gamma)} = 0$ and $r_N^{(\beta\gamma)} = r_T^{(\beta\gamma)} \rightarrow \infty$ correspond to perfect bonding and complete separation, respectively. It is also possible to specify $r_N^{(\beta\gamma)}$ and $r_T^{(\beta\gamma)}$ as evolving functions of the interfacial tractions, see Wang et al. [13], for example, which results in evolving interfacial damage. Conditions (38) and (39) provide another $3(N_\beta - 1)N_\gamma + 3N_\beta(N_\gamma - 1)$ equations.

Finally, the periodicity conditions that require the equality of the surface-average displacement and traction increments at the opposite sides of the repeating unit cell are

$$\begin{aligned} [\Delta \mathbf{u}_2 \ \Delta \mathbf{T}_2]^{-(1\gamma)} &= [\Delta \mathbf{u}_2 \ \Delta \mathbf{T}_2]^{+(N_\beta\gamma)}, \quad \gamma = 1, \dots, N_\gamma \\ [\Delta \mathbf{u}_3 \ \Delta \mathbf{T}_3]^{-(\beta 1)} &= [\Delta \mathbf{u}_3 \ \Delta \mathbf{T}_3]^{+(\beta N_\gamma)}, \quad \beta = 1, \dots, N_\beta \end{aligned} \quad (40)$$

which form additional $6N_\beta + 6N_\gamma$ equations.

Consequently, Eqs. (37)–(40) form a system of $12N_\beta N_\gamma$ algebraic equations in the same number of the surface-average displacement increments $\Delta \mathbf{u}^{\pm(\beta\gamma)}$ in the entire repeating unit cell (namely the composite). The solution at a current loading increment establishes the fourth-order instantaneous stress concentration tensor $\mathbf{A}^{(\beta\gamma)}$, which relates the increment of the local deformation gradient (in the subcell) $\Delta \mathbf{F}^{(\beta\gamma)}$ to the current

externally applied far-field global deformation gradient increment $\Delta\bar{\mathbf{F}}$, namely,

$$\Delta\mathbf{F}^{(\beta\gamma)} = \mathbf{A}^{(\beta\gamma)} : \Delta\bar{\mathbf{F}} \quad (41)$$

The average stress increments in the composite are given by

$$\Delta\bar{\mathbf{T}} = \frac{1}{HL} \sum_{\beta=1}^{N_\beta} \sum_{\gamma=1}^{N_\gamma} h_{\beta} l_{\gamma} \Delta\mathbf{T}^{(\beta\gamma)} \quad (42)$$

Substituting the incremental constitutive equation (17) for $\Delta\mathbf{T}^{(\beta\gamma)}$ and employing Eq. (41) establishes in the macroscopic (global) incremental constitutive equation of the composite

$$\Delta\bar{\mathbf{T}} = \mathbf{R}^* : \Delta\bar{\mathbf{F}} \quad (43)$$

where \mathbf{R}^* is the effective instantaneous fourth-order first tangent tensor of the composite which is given by

$$\mathbf{R}^* = \frac{1}{HL} \sum_{\beta=1}^{N_\beta} \sum_{\gamma=1}^{N_\gamma} h_{\beta} l_{\gamma} \mathbf{R}^{(\beta\gamma)} \mathbf{A}^{(\beta\gamma)} \quad (44)$$

In conclusion, the HFGMC micromechanical method has established the macroscopic constitutive equations, which govern the behavior of multiphase composites that are composed of hyperelastic material characterized by softening effects which lead to loss of static stability. This loss of static stability in a subcell which is filled by a hyperelastic material affects the composite response and indicates the occurrence of the initiation of failure in the composite.

4 Verification of the HFGMC Micromechanical Prediction: Axisymmetric Loading

The reliability of the finite strain HFGMC predicted macroscopic response has been verified in Refs. [8,9], by considering a hollow cylinder under externally applied radial stretch and zero axial deformation for which exact analytical solutions can be developed for several types of nonlinearly elastic materials with substantially different stiffening and softening behavior. These hyperelastic materials include two harmonic materials discussed by Ogden [10] and Jafari et al. [14], henceforth called Ogden and JAH materials, Varga material discussed by Haughton [15], and Blatz and Ko [16] material. These analytical solutions have been summarized and reviewed by Horgan [17,18].

The employed cylindrical geometry and loading correspond to the response of the concentric cylinder assemblage (CCA) model proposed by Hashin and Rosen [19] which in the present context represents a porous composite with a dilute axial pore content subjected to large axisymmetric deformations. In the framework of this model, the radial stress–radial stretch ($T_{RR} - \lambda_{RR}$) response of the outer surface of a single hollow cylinder subjected to axisymmetric loading coincides with that of the effective response ($\bar{T}_{RR} - \bar{\lambda}_{RR}$) of the entire porous composite subjected to the same type of loading. The hollow core accounts for only 5% of the total cross-sectional area transverse to the reinforcement direction, allowing a direct comparison with the present micromechanical model predictions based on the repeating unit cell with 5% void fraction subjected to biaxial tension $\bar{F}_{22} = \bar{F}_{33}$ that provides $\bar{T}_{22} = \bar{T}_{33}$. A direct comparison between \bar{T}_{RR} and $\bar{T}_{22} = \bar{T}_{33}$ provides information about the accuracy of the micromechanical prediction. It should be emphasized that the offered reliability verification is meaningful because although the CCA problem is one-dimensional, the present micromechanical doubly periodic model is two-dimensional. The specific discretization of the repeating unit cell that mimics the circular character of the central void surrounded by the nonlinear material is given in Ref. [8]. The two approaches differ also in the sense that whereas the finite

strain HFGMC analysis is based on a tangential formulation, the CCA equations shown in the following are based on the total value of the field variables rather than their increments.

In the present case of a hyperelastic material with a limiter namely, with a strain-energy function of the form given by Eq. (3), these analytical solutions are not valid anymore. They are applicable only in the case of $\phi \rightarrow \infty$. With the axisymmetric loading of cylindrical geometry, it is possible however to solve the one-dimensional equilibrium equations for these materials by a two-point finite difference procedure and compare the resulting solution with the HFGMC prediction to verify its accuracy. This approach is discussed in the following.

4.1 Axisymmetric Loading of a Hollow Cylinder. Consider the plane strain deformation of a hollow cylinder under a uniform radial stretch at the outer radius and zero tractions at the inner radius. Let R and Θ denote the polar coordinates of a material particle in the initial configuration, where $A \leq R \leq B$, $0 \leq \Theta \leq 2\pi$ with A and B denoting the inner and outer radii, respectively. The current location of this particle is given by r and θ such that the deformation is described by $r(R)$ and $\theta = \Theta$, where $a \leq r(R) \leq b$ and a and b denote the current inner and outer radii.

For this type of deformation, the deformation gradient is given by

$$\mathbf{F} = \text{diag} \left(\frac{dr(R)}{dR}, \frac{r(R)}{R}, 1 \right) \quad (45)$$

and the principal stretches λ_1 , λ_2 , and λ_3 are given by

$$\lambda_1 = \frac{dr(R)}{dR}, \quad \lambda_2 = \frac{r(R)}{R}, \quad \lambda_3 = 1 \quad (46)$$

The equilibrium equations reduce to the single equation

$$\frac{dT_{RR}}{dR} + \frac{T_{RR} - T_{\Theta\Theta}}{R} = 0 \quad (47)$$

where T_{RR} and $T_{\Theta\Theta}$ are the components of the first Piola–Kirchhoff stress tensor. With the enhanced strain-energy function ψ given by Eq. (3), these components are given by

$$T_{RR} = \frac{\partial W}{\partial \lambda_1} \exp(-W^m/\phi^m), \quad T_{\Theta\Theta} = \frac{\partial W}{\partial \lambda_2} \exp(-W^m/\phi^m) \quad (48)$$

Consequently, Eq. (47) reduces to the nonlinear ordinary differential equation

$$\left[\frac{\partial^2 W}{\partial \lambda_1^2} - \left(\frac{\partial W}{\partial \lambda_1} \right)^2 \frac{m}{\phi^m} W^{m-1} \right] \frac{d^2 r}{dR^2} + \left[\frac{\partial^2 W}{\partial \lambda_1 \lambda_2} - \frac{\partial W}{\partial \lambda_1} \frac{\partial W}{\partial \lambda_2} \frac{m}{\phi^m} W^{m-1} \right] \times \left(\frac{1}{R} \frac{dr}{dR} - \frac{r}{R^2} \right) + \frac{1}{R} \left(\frac{\partial W}{\partial \lambda_1} - \frac{\partial W}{\partial \lambda_2} \right) = 0 \quad (49)$$

The solution for $r(R)$, which depends on the particular form of the strain-energy W , is obtained subject to the traction-free condition at the inner radius, and specified deformation at the outer radius in the current configuration, i.e.,

$$\begin{aligned} T_{RR} &= 0, & R &= A \\ r(B) &= b = \bar{\lambda}_{RR} B, & R &= B \end{aligned} \quad (50)$$

where $\bar{\lambda}_{RR}$ is the prescribed radial stretch.

The determination of $r(R)$ leads to the determination of the stresses, including the radial stress T_{RR} at the outer surface $R = B$. The use of the average stress theorem (for example see Ref. [4]) produces the average radial stress \bar{T}_{RR} for the entire hollow cylinder, namely, $\bar{T}_{RR} = T_{RR}(R = B)$. Consequently, the effective

stress–deformation relationship of the porous material, with the initial volume concentration of pores given by $A^2/B^2 < 1$, subjected to the specified plane strain axisymmetric loading by $\lambda_{RR} = b/B$, is established.

The second-order nonlinear ordinary differential equation, Eq. (49), and the boundary conditions, Eq. (50), form a two-point boundary value problem. As stated before, for the above four types of hyperelastic materials exact solutions can be derived, when $\phi \rightarrow \infty$ only. Solutions of this equation in the general case can be obtained by employing a finite-difference procedure for two-point boundary value problems. According to this method, the interval $A \leq R \leq B$ is divided into several subintervals and the derivatives are replaced by their corresponding finite differences in these intervals. As a result, a system of nonlinear algebraic equations is obtained which is solved by an iterative procedure until convergence is achieved up to a pre-assigned degree of accuracy.

4.2 Ogden Harmonic Material. Results are given herein for the following strain-energy function that was proposed by Ogden [10]:

$$W = \frac{2\nu - \mu}{27}(\lambda_1 + \lambda_2 + 1)^3 + \nu - \nu(\lambda_1\lambda_2 + \lambda_1 + \lambda_2) + \mu\lambda_1\lambda_2 \quad (51)$$

with the material constants $\nu = 1$ MPa and $\mu = -4$.

In the special case, when $\phi \rightarrow \infty$ the exact of Eq. (49) is given by

$$r(R) = PR + \frac{Q}{R} \quad (52)$$

where P and Q are coefficients that can be determined from the boundary conditions (50).

In Fig. 2(a), the first Piola–Kirchhoff stress variations with deformation gradient, caused by the application of simple tension in the two-direction of the monolithic material, are shown for $\phi \rightarrow \infty$ and $\phi = 5$ MPa, $m = 10$. The effect of the limiters addition is clearly exhibited. In Fig. 2(b), comparisons between the stresses based on the exact CCA solution given by Eq. (52), the finite difference solution of Eq. (49) and HFGMC prediction of the porous material are shown in the absence of a limiter, i.e., $\phi \rightarrow \infty$. Excellent agreements between the three methods are noticed. Finally, a comparison between the finite difference solution and HFGMC predictions of the porous material are shown in Fig. 2(c). The HFGMC prediction, which is based on tangential formulation, can be seen to be valid up to the critical point of ψ^c of the the strain-energy ψ where it coincides with the CCA finite difference solution. On the other hand, the finite difference solution, based on a total formulation, is capable to predict the solution a little farther.

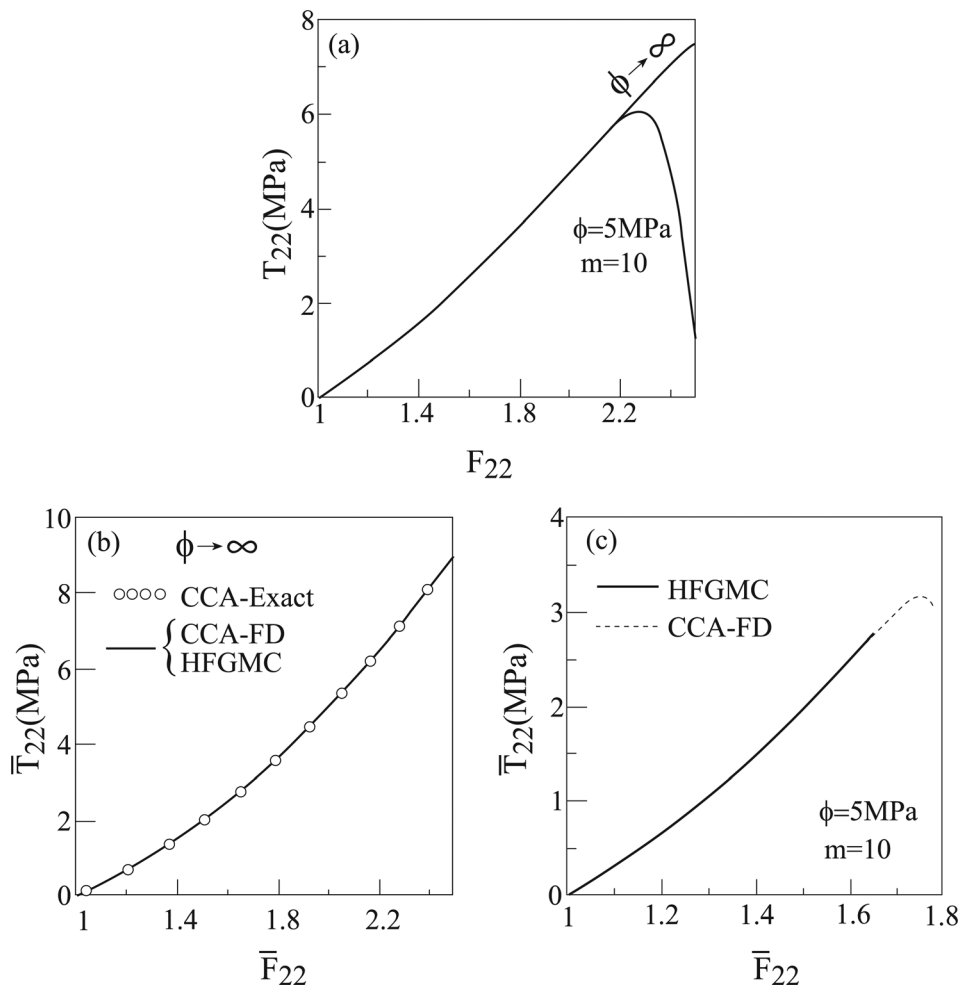


Fig. 2 (a) The response of the monolithic Ogden harmonic material to simple tension in the two-direction. (b) The macroscopic response of porous Ogden material subjected to a biaxial loading. Comparison between the HFGMC, exact CCA, and finite difference solutions for $\phi \rightarrow \infty$. (c) The macroscopic response of porous Ogden material subjected to a biaxial loading. Comparison between the HFGMC and finite difference solutions for $\phi = 5$ MPa and $m = 10$.

4.3 JAH Harmonic Material. This harmonic material is characterized by the strain-energy function which has been specified by Jafari et al. [14] as

$$W = 2\mu \left[\frac{(\lambda_1 + \lambda_2)^2}{2} + \frac{\lambda_1 + \lambda_2}{\nu - 1} \left(\frac{2}{\lambda_1 + \lambda_2} \right)^\nu + \frac{1 + \nu}{1 - \nu} - \lambda_1 \lambda_2 \right],$$

$$\nu \geq 0, \quad \nu \neq 1, \quad \lambda_1 + \lambda_2 > 0 \quad (53)$$

with the material constants $\mu = 1$ MPa and $\nu = 1.5$. Here too the solution of Eq. (49) for $\phi \rightarrow \infty$ is given by Eq. (52). As in the previous case, Figs. 3(a)–3(c) exhibit the monolithic material response in simple tension, the porous material response when $\phi \rightarrow \infty$ and its response for $\phi = 1$ MPa and $m = 10$. Excellent agreements between the solutions are clearly observed.

4.4 Blatz and Ko Material. The final verification is presented for the Blatz and Ko material [16], which is characterized by the strain-energy function

$$W = \frac{\mu}{2} [\lambda_1^{-2} + \lambda_2^{-2} + 2\lambda_1 \lambda_2 - 4] \quad (54)$$

with the material constant $\mu = 1$ MPa. In the limiting case of $\phi \rightarrow \infty$, the solution of Eq. (49) has been derived from that presented by Chung et al. [20] for the finite deformation of internally pressurized cylinder which was modified in Ref. [8] for the

boundary conditions given by Eq. (50). The monolithic material behavior under simple tension in the two-direction with and without limiter is shown in Fig. 4(a), and the resulting comparisons of the porous material responses are shown in Figs. 4(b) and 4(c) for $\phi \rightarrow \infty$ and $\phi = 0.2$ MPa, $m = 10$.

5 Applications

Applications are given herein for filled natural rubber reinforced by unidirectional nylon fibers. The rubber matrix was characterized by Hamdi et al. [21] by employing Yeoh [22] hyperelastic strain-energy function which is given by

$$W = \sum_{k=1}^3 C_k (\lambda_1^2 + \lambda_2^2 + \lambda_3^2 - 3)^k \quad (55)$$

where the constants are: $C_1 = 0.298$ MPa, $C_2 = 0.014$ MPa, and $C_3 = 0.00016$ MPa. In addition, Hamdi et al. [21] observed that failure of the material in simple tension in the one-direction occurs when the value of the stretch is $\lambda_1 = 7.12$. The resulting response was calibrated by Ref. [6] to determine the values of ϕ and m in Eqs. (4) and (5). The recommended values $\phi = 82$ MPa and $m = 10$ have been chosen in the present article. This value of ϕ has been obtained by a fit with the uniaxial tension test of Hamdi et al. [21]. The corresponding critical strain-energy is $\psi^c = 63.1$ MPa, and the energy of separation which is given by Eq. (4) is 78 MPa.

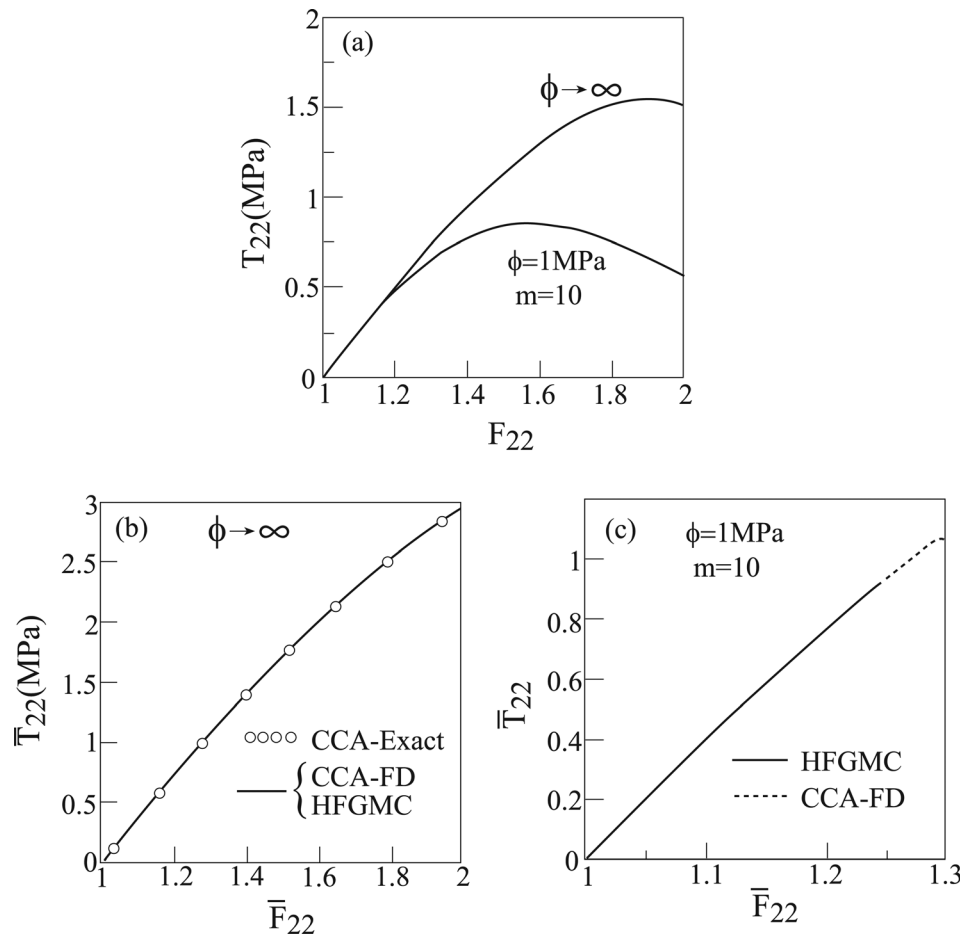


Fig. 3 (a) The response of the monolithic JAH harmonic material to simple tension in the two-direction. (b) The macroscopic response of porous Ogden material subjected to a biaxial loading. Comparison between the HFGMC, exact CCA, and finite difference solutions for $\phi \rightarrow \infty$. (c) The macroscopic response of porous JAH material subjected to a biaxial loading. Comparison between the HFGMC and finite difference solutions for $\phi = 1$ MPa and $m = 10$.

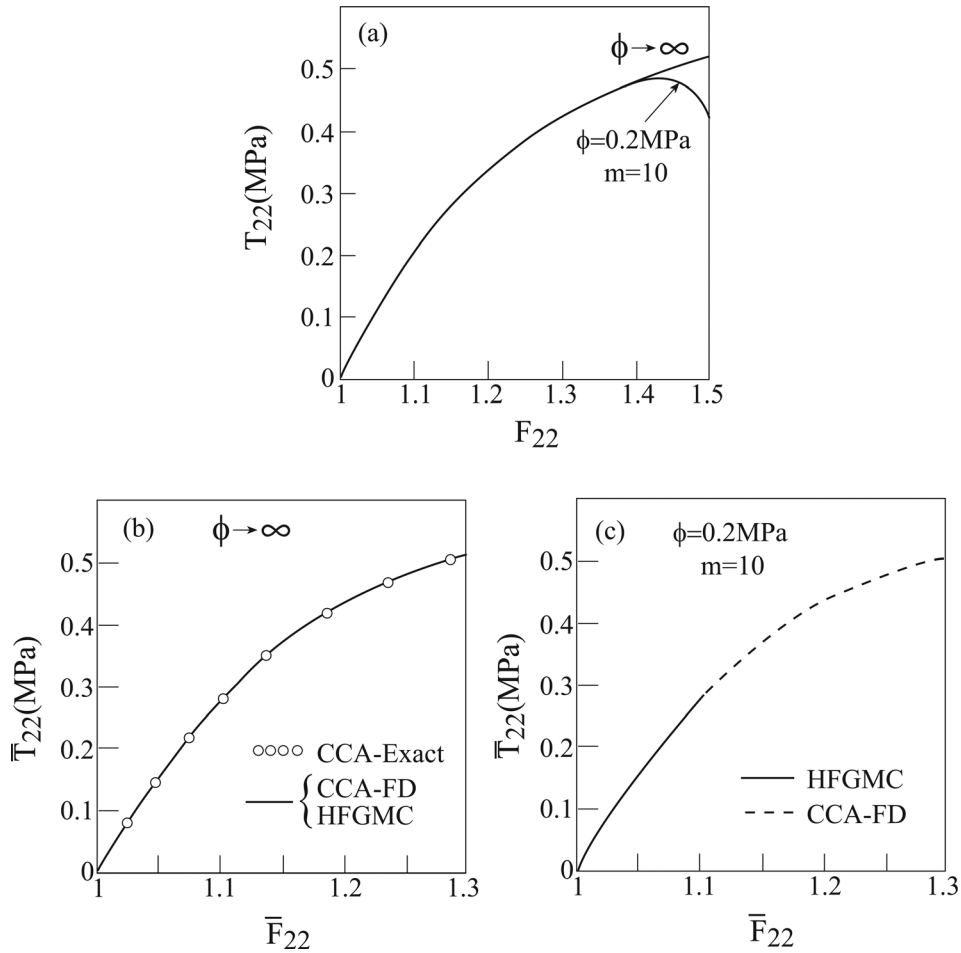


Fig. 4 (a) The response of the monolithic Blatz and Ko material to simple tension in the two-direction. (b) The macroscopic response of porous Blatz and Ko material subjected to a biaxial loading. Comparison between the HFGMC, exact CCA, and finite difference solutions for $\phi \rightarrow \infty$. (c) The macroscopic response of porous Blatz and Ko material subjected to a biaxial loading. Comparison between the HFGMC and finite difference solutions for $\phi = 0.2 \text{ MPa}$ and $m = 10$.

The failure of rubber and abdominal aortic aneurysm have been discussed by Volokh [6,7], respectively. It turned out that failure based on the critical value ψ^c of the strain-energy ψ is advantageous over other criteria such as the critical stretch, stress, shear stress, or von Mises. Therefore, this energy based criterion at

which static stability is lost is adopted in the present article as an indicator for the onset of failure.

Equation (55) represents an incompressible material in which $J = \lambda_1 \lambda_2 \lambda_3 = 1$. It is more convenient to employ a compressible version of Eq. (55) which is given by

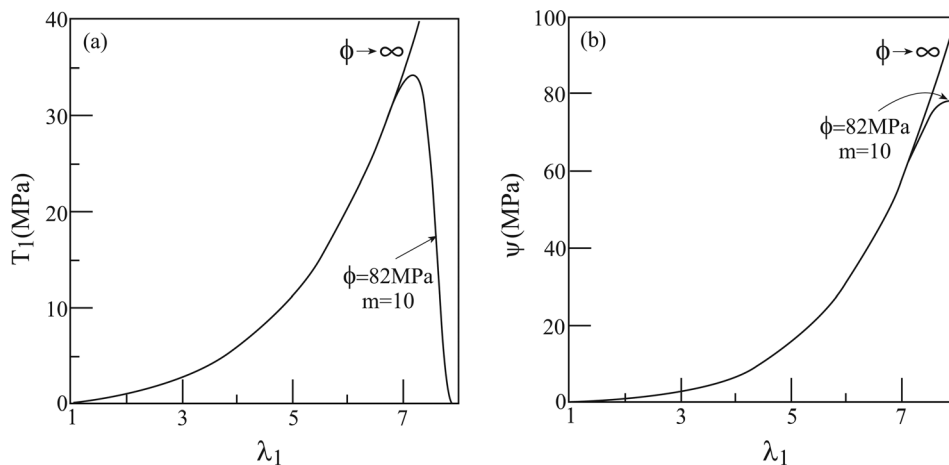


Fig. 5 The response of the monolithic matrix described by Eq. (56) to simple tension in the one-direction. (a) Piola-Kirchhoff stress T_1 and (b) strain-energy ψ .

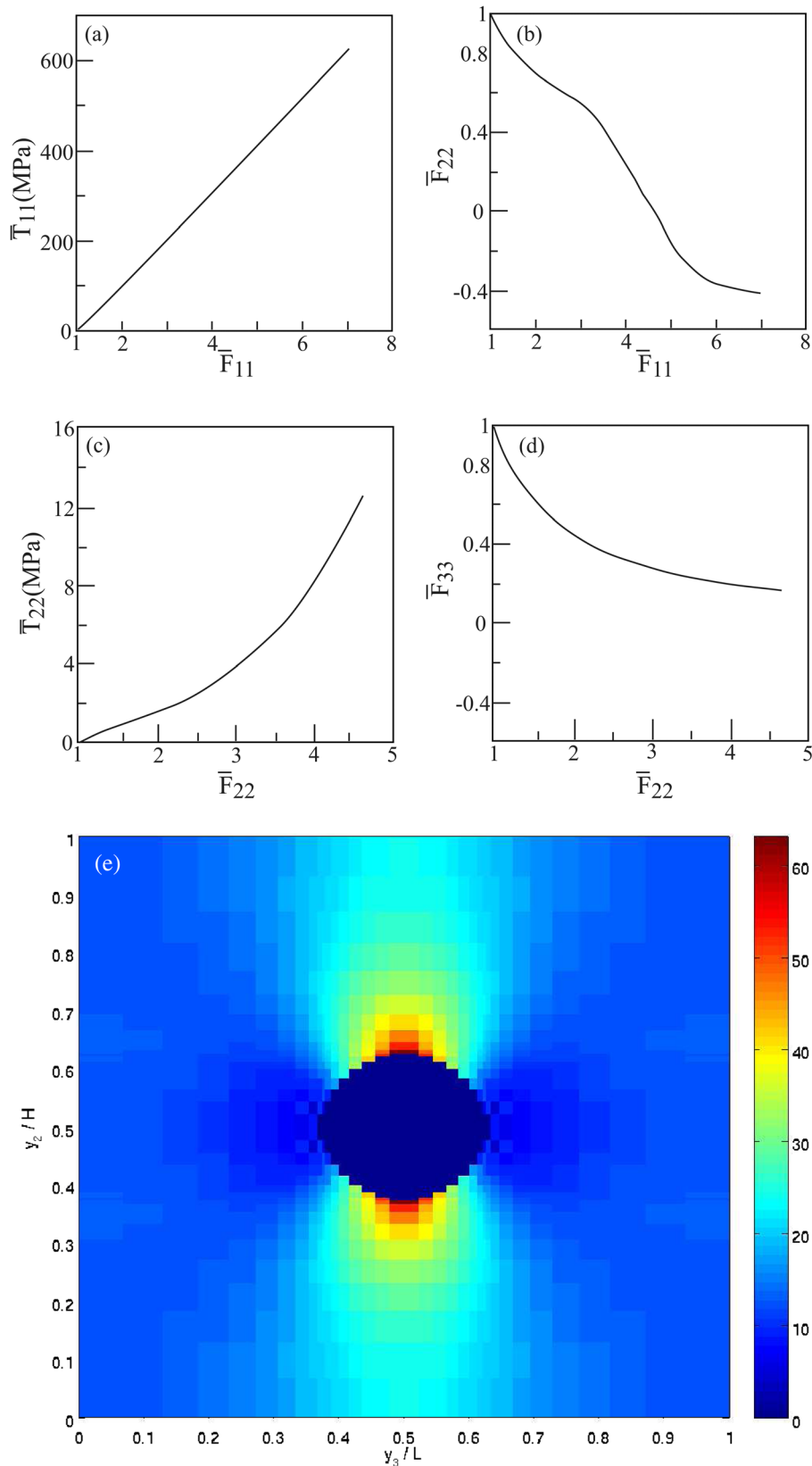


Fig. 6 (a) Stress–deformation gradient response of the nylon/rubberlike composite to uniaxial stress loading in the fibers direction and (b) the induced deformation gradient in the transverse direction. (c) Stress–deformation gradient response of the composite to uniaxial stress loading in the transverse direction and (d) the induced deformation gradient in the other transverse direction. (e) The distribution in the repeating unit cell $0 \leq Y_2/H \leq 1, 0 \leq Y_3/L \leq 1$ of the strain-energy ψ when $\psi = \psi^c = 63.1$ MPa.

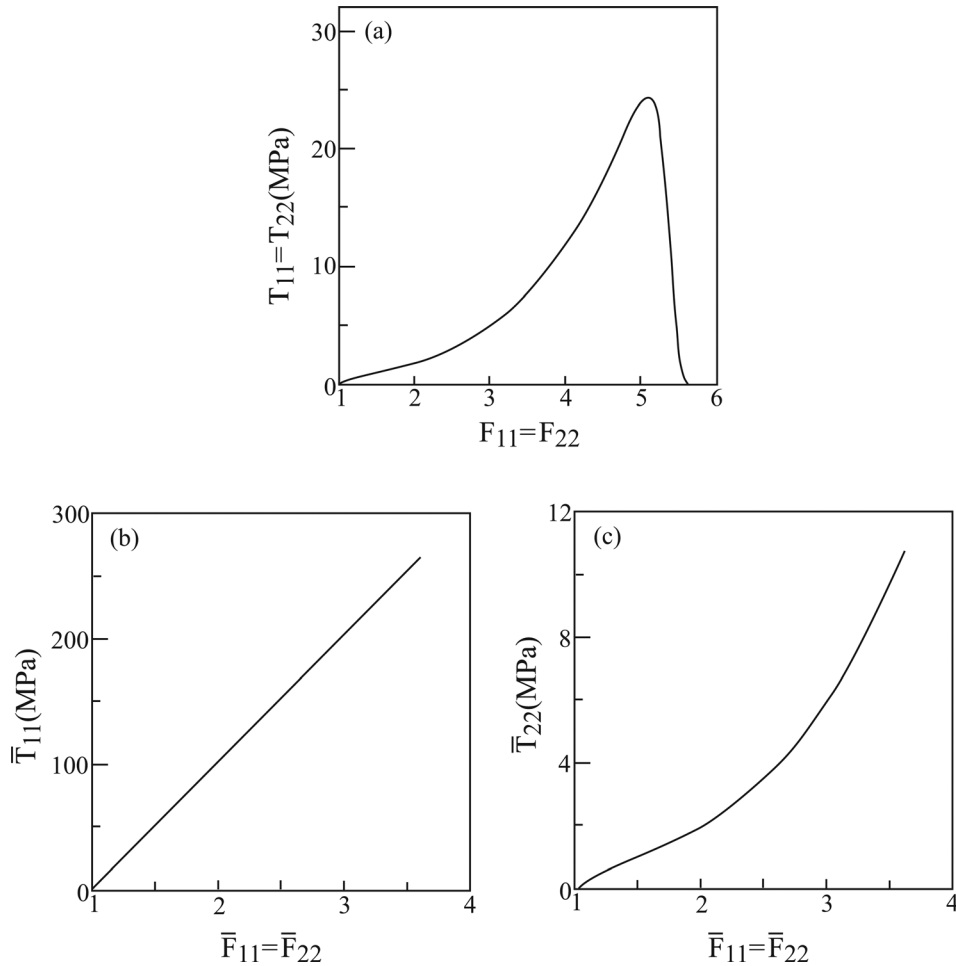


Fig. 7 (a) Stress–deformation gradient response of the unreinforced matrix caused by the application of a biaxial loading. (b) Macroscopic axial stress and (c) transverse stress against deformation gradient of the nylon/rubberlike composite. The composite is subjected to equal axial and transverse loading while keeping all other global stress components equal to zero.

$$W = \sum_{k=1}^3 C_k (\bar{\lambda}_1^2 + \bar{\lambda}_2^2 + \bar{\lambda}_3^2 - 3)^k + \kappa (J - 1)^2 \quad (56)$$

where $\bar{\lambda}_k = \lambda_k / J^{1/3}$ and κ represent the bulk modulus such that a nearly incompressible material is obtained for large values of κ . In the characterization of Yeoh material by the compressible version given by Eq. (56), the value of $\kappa = 1 \text{ GPa}$ has been chosen which turns out to yield a determinant of the deformation gradient which is very close to unity during the deformation process. Figure 5 exhibits the variations of the Piola–Kirchhoff stress and the strain-energy ψ for $\phi = 82 \text{ MPa}$ and $m = 10$ caused by the application of a simple tension in the one-direction.

Remark. It should be noted that the strain-energy (56) can be also represented in the form

$$W = \sum_{k=1}^3 C_k (\bar{I}_1 - 3)^k + \kappa (J - 1)^2 \quad (57)$$

where $\bar{I}_1 = I_1 / J^{2/3}$, $I_1 = \text{tr}(\mathbf{C})$ being the first invariant of the right Cauchy–Green strain tensor \mathbf{C} and $J = \det(\mathbf{F})$. The enhanced strain-energy function is given by Eq. (9). By evaluating the first and second derivatives of \bar{I}_1 and J with respect to the components of \mathbf{C} and by using the relation $\partial\psi/\partial W = \exp(-W^m/\phi^m)$, the tangent tensor \mathbf{D} in Eq. (13) can be established according to

$$D_{ijkl} = 4 \frac{\partial^2 \psi}{\partial C_{ij} \partial C_{kl}}, \quad i, j, k, l = 1, 2, 3 \quad (58)$$

from which Eqs. (15)–(18) follow.

The nylon fibers are assumed to be linearly elastic and isotropic (although the HFGMC method allows combinations with one or more different hyperelastic materials) with Young’s modulus and Poisson’s ratio given by 2 GPa and 0.4, respectively.

Let the rubberlike matrix be reinforced by unidirectional fibers. The fibers are oriented in the X_1 -direction which is referred to as the axial direction. The volume fraction of the fibers is chosen as $v_f = 0.05$ which is characteristic of fiber-reinforced rubber. As in the three verifications discussed above, the repeating unit cell has been discretized into 36×36 subcells appropriately dimensioned to mimic a void in porous materials and a circular fiber in a fiber-reinforced composite.

5.1 Perfect Bonding Between Fibers and Matrix. In

Figs. 6(a) and 6(b), the composite response to uniaxial stress loading is shown by the macroscopic first Piola–Kirchhoff stress \bar{T}_{11} and global transverse deformation gradient \bar{F}_{22} against the global axial deformation gradient \bar{F}_{11} , respectively. As expected, the uniaxial stress loading of the composite in the fibers direction generates a linear macroscopic response, since the fibers which are much stiffer than the rubber matrix carries most of the loading.

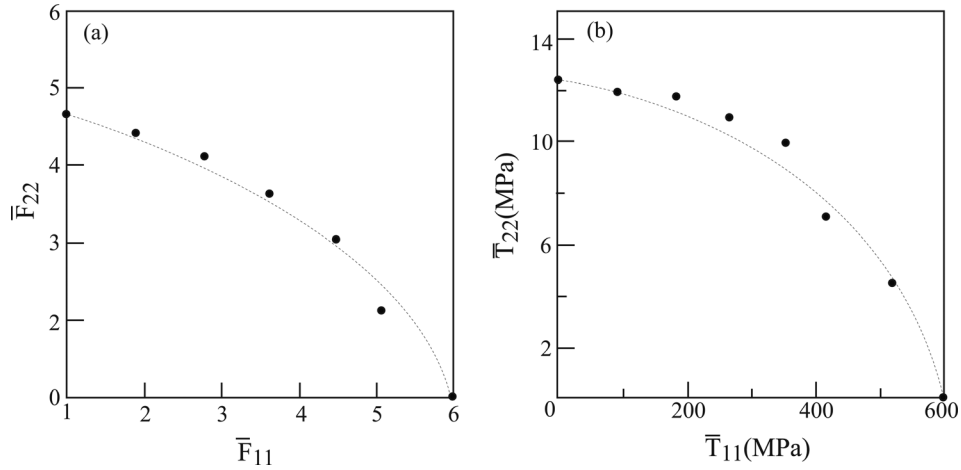


Fig. 8 Biaxial loading of nylon/rubberlike composite. (a) Initial failure envelope in the plane $\bar{F}_{11} - \bar{F}_{22}$. (b) Initial failure envelope in the plane $\bar{T}_{11} - \bar{T}_{22}$.

The failure of the composite occurs when the strain-energy in a matrix subcell reaches the aforementioned critical value $\psi^c = 63.1$ MPa at which $\bar{F}_{11} = 6.8$. The value of the induced stress within the fiber subcells at $\bar{F}_{11} = 6.8$ is about 12 GPa. This value far exceeds the ultimate stress of the nylon fibers which is in the range of 80 – 185 MPa. Hence, the fibers will be broken at a strain of about 0.1, see Assaad and Arnold [23].

The composite response to uniaxial transverse stress loading exhibits, on the other hand, an entirely different behavior which is shown in Figs. 6(c) and 6(d). These two figures show the macroscopic first Piola–Kirchhoff transverse stress \bar{T}_{22} and deformation gradient \bar{F}_{33} against the applied global transverse deformation gradient \bar{F}_{22} . The resulting much lower stress values up to failure occurrence at $\bar{F}_{22} = 4.7$ (where the strain-energy in a matrix reaches its critical value) reflects the matrix deformation dominance in the present type of loading. It is interesting to exhibit in the present case of uniaxial transverse loading the resulting distribution of the strain-energy ψ in the repeating unit cell $0 \leq Y_2/H \leq 1, 0 \leq Y_3/L \leq 1$ at the failure point, where the critical value $\psi = 63.1$ MPa is reached. This distribution is shown in

Fig. 6(e). It can be readily observed that the highest values of ψ are detected in the same locations where the largest stress concentrations are expected. It should be noted that the induced stresses within the fibers at the instant of failure do not reach their ultimate stress value. Thus, the fibers remain intact when the first matrix subcell fails.

Let us consider a biaxial loading of the composite in the axial and transverse directions while keeping the stress in the other normal direction equal to zero (i.e., $\bar{T}_{33} = 0$) as well all other shear stresses. Figure 7(a) shows the stress behavior of the monolithic (unreinforced) matrix to this type of loading. The critical failure value $\psi^c = 63.1$ MPa occurs at $F_{11} = F_{22} = 5$ (rather than at 7.12 in the simple tension case). The corresponding composite response to this type of loading is shown in Figs. 7(b) and 7(c). These figures exhibit the macroscopic stresses \bar{T}_{11} and \bar{T}_{22} in the axial and transverse directions. Here, the failure of a matrix subcell occurs at $\bar{F}_{11} = \bar{F}_{22} = 3.6$ which is quite lower than the critical stretch of the unreinforced matrix. This lower value results from the combined system of stresses which act on the matrix advancing its initial failure.

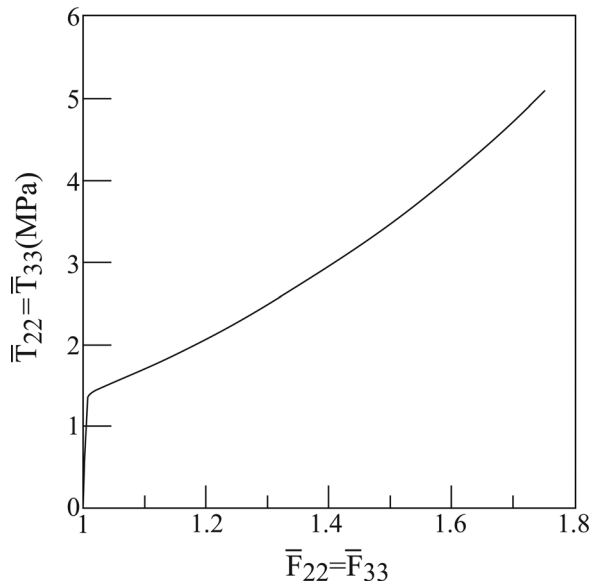


Fig. 9 Stress–deformation gradient response of the nylon/rubberlike composite to biaxial loading in both transverse directions

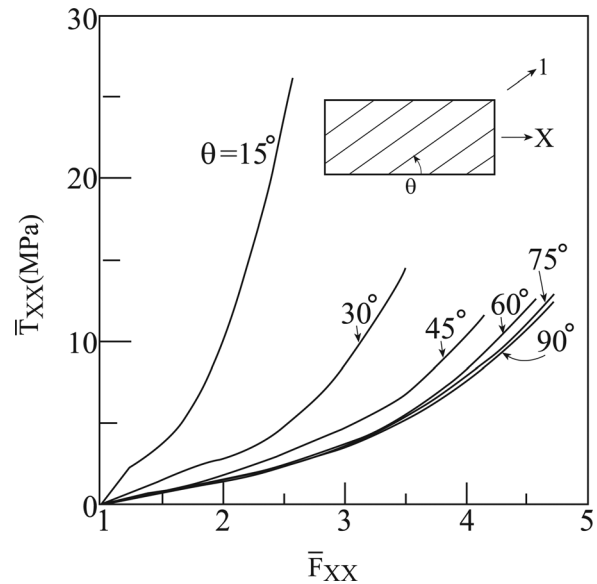


Fig. 10 Axial response to off-axis unidirectional nylon/rubberlike composite. The rotation θ around three-direction denotes the angle between the fibers (oriented in the one-direction) and loading (applied in the X-direction).

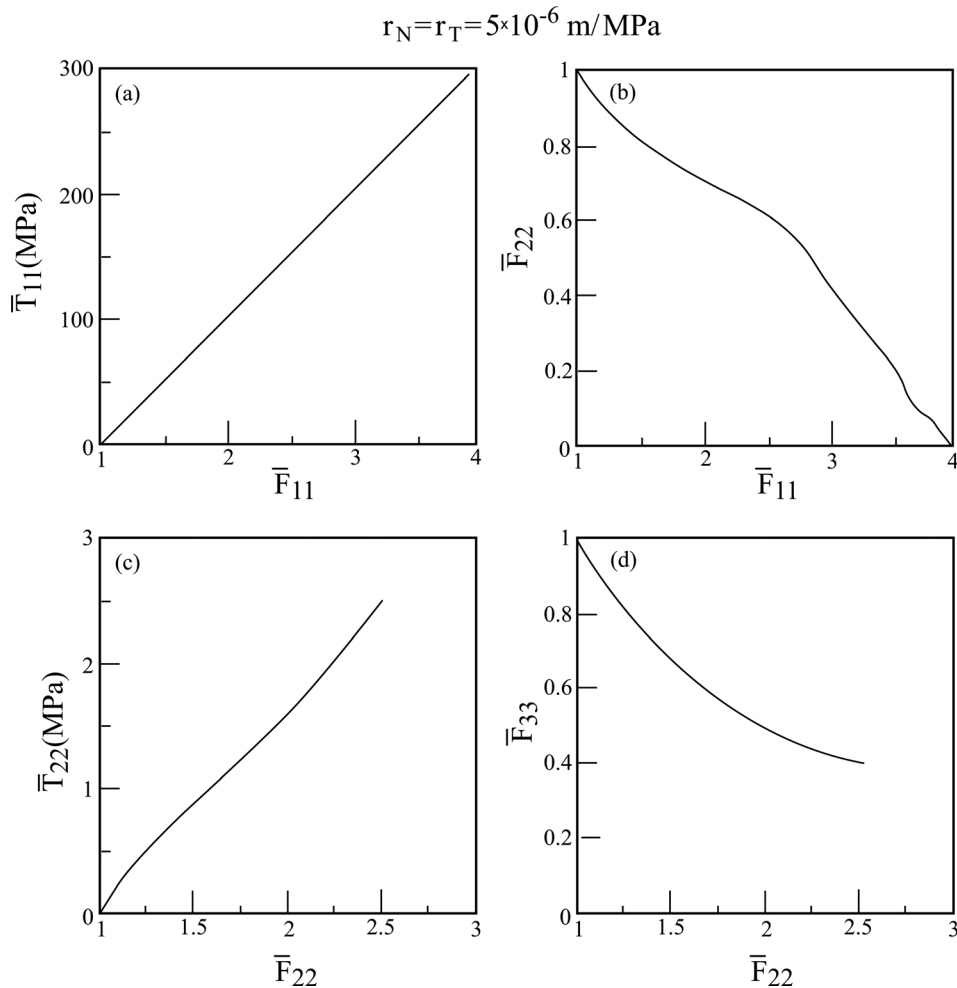


Fig. 11 Nylon/rubberlike composite in the presence of imperfect bonding of $r_N = r_T = 5 \times 10^{-6} \text{ m/MPa}$. (a) Stress–deformation gradient response of the nylon/rubberlike composite to uniaxial stress loading in the fibers direction and (b) the induced deformation gradient in the transverse direction. (c) Stress–deformation gradient response of the composite to uniaxial stress loading in the transverse direction and (d) the induced deformation gradient in the other transverse direction.

It should be useful to generate initial failure envelopes when the composite is subjected to a combined biaxial loading such that

$$\Delta \bar{F}_{11} = A \cos \omega, \quad \Delta \bar{F}_{22} = A \sin \omega, \quad 0 \leq \omega \leq \pi/2 \quad (59)$$

where A is an amplitude value which incrementally increases until failure in a matrix subcell occurs. Just like the previous case, the macroscopic stress \bar{T}_{33} and all other shear stresses are kept equal to zero. Figures 8(a) and 8(b) show the resulting initial failure envelopes in the planes of the global deformation gradients $\bar{F}_{22} - \bar{F}_{11}$ and stresses $\bar{T}_{22} - \bar{T}_{11}$, respectively. Additional two points in these graphs have been added from axial and transverse uniaxial stress loading cases. It should be noted that due to the very strong directivity of the stress envelope shown in Fig. 8(b), the scale ratio is taken as 1 : 40. Figure 8(b) well exhibits the effect of reinforcement on the composite response in this type of combined loading. The corresponding case of a combined loading applied on the unreinforced rubber exhibits a circular envelope in the stretch plane $\lambda_1 - \lambda_2$ of a radius of 7.12 [6].

Biaxial loading of the composite in both transverse directions, i.e., $\bar{F}_{22} = \bar{F}_{33}$ (with the global stresses in all other directions are kept equal to zero) reveals a quite different situation. The resulting equal macroscopic transverse stresses $\bar{T}_{22} = \bar{T}_{33}$ are shown in Fig. 9. First failure of the matrix is seen to take place at

$\bar{F}_{22} = \bar{F}_{33} = 1.75$ which is quite low indicating that the ability of the composite to sustain loading in this case is limited as compared to the previous loadings.

The next illustration is presented in the case of off-axis loading. Here, the material coordinates with respect to which the fibers of the unidirectional composite are oriented in the one-direction, is rotated around the three-direction by an angle θ . As a result, a new system of coordinates (X, Y, Z) is obtained such that $Z = X_3$. A uniaxial stress loading is applied in the X -direction which is at angle θ with respect to the fibers direction. With respect to the material coordinates, this results into a combined loading acting on the composite. Referring to this new system of coordinates, the composite is loaded by the application of the deformation gradient \bar{F}_{XX} , and all components of the stress \bar{T}_X , referred to the new coordinate system, are kept equal to zero (except of course \bar{T}_{XX}). In particular, $\theta = 0 \text{ deg}$ and 90 deg correspond to axial and transverse uniaxial stress loading, respectively, that have been discussed in Fig. 6. Figure 10 shows the resulting response to off-axis uniaxial stress loading at various off-axis angles θ . The end point in every curve corresponds to the failure of the first matrix subcell. It can be observed that initial failure can be delayed by increasing the off-axis angle but with lower ability to sustain high stresses. Multidirectional reinforcements by lamination would improve of course the composite effectiveness.

$$r_N = r_T = 5 \times 10^{-6} \text{ m/MPa}$$

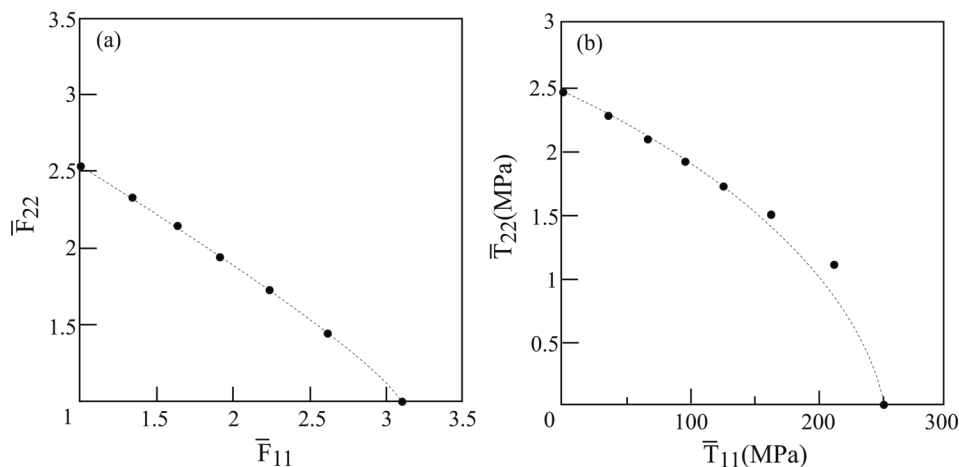


Fig. 12 Biaxial loading of nylon/rubberlike composite in the presence of imperfect bonding of $r_N = r_T = 5 \times 10^{-6} \text{ m/MPa}$. (a) Initial failure envelope in the plane $\bar{F}_{11} - \bar{F}_{22}$. (b) Initial failure envelope in the plane $\bar{T}_{11} - \bar{T}_{22}$.

5.2 Imperfect Bonding Between Fibers and Matrix. The previous results were generated by assuming that perfect bonding between the fibers and rubberlike matrix constituents exists (i.e., $r_N = r_T = 0$ in Eqs. (38) and (39)). In the following, results are given in the case of a weak bonding caused by manufacturing, thermal treatment, fabrication process, or during service. In Fig. 11, the response of the composite to uniaxial stress loading in the axial and transverse directions is shown by assuming that the compliance parameters are: $r_N = r_T = 5 \times 10^{-6} \text{ m/MPa}$. This figure is the counterpart of Fig. 6 with perfect bonding. A comparison between the two figures reveals that this degree of imperfection caused a tremendous deterioration of the composite's reinforcing capability. The failure of the composite loaded in fiber direction reduced both global deformation gradient and macroscopic stress by about 0.5. It should be noted that here too, the nylon fibers would reach their ultimate stress at a strain of about 0.1. In the uniaxial transverse loading case, the reductions of deformation gradient and stress with respect to the perfect bonding case are about 0.5 and 0.2, respectively. This implies that the effect of imperfect bonding in this case is more severe.

The corresponding to the initial failure envelopes that were shown in Fig. 8 are given in the present case in Fig. 12. These envelopes have been generated by applied a series of biaxial loading in the axial and transverse directions, Eq. (59), with vanishing other stress components. As in Fig. 8, two additional points were taken from the previous axial and transverse loading cases. A comparison of this figure with Fig. 8 illustrates the effect of the present degree of imperfection on the composite response.

Finally, it should be emphasized that the stress-strain response for perfect and imperfect bonding is different not only quantitatively but also qualitatively. Indeed, the bottom left curve in Fig. 6 is typical of rubber behavior because it exhibits stiffening (due to unfolding of long molecules). Thus, the rubber dominates the deformation. To the contrary, the bottom left curve in Fig. 11 is much straighter because the interface compliance affects the deformation significantly.

6 Conclusions

By the incorporation of hyperelastic strain-energy functions with limiters with the finite strain HFGMC micromechanical method, macroscopic constitutive equations which govern the behavior of composites undergoing large deformations have been established. The resulting micromechanical analysis is capable of

predicting the onset of local loss of static stability in the hyperelastic constituent which leads to the composite initial failure. Failure initiation is based on the critical value of the strain-energy function to which the local strain-energy is approached. Various types of loading have been examined and initial failure envelope has been presented. In addition, the capability of modeling weak bonding between fibers and matrix has been included, and the resulting effect on the composite response and initial failure envelope has been illustrated.

It should be emphasized that HFGMC method does not only predicts the effective moduli of linearly elastic composites and establishes the macroscopic constitutive equations of composites undergoing large deformations, but it also provides the field distribution in the entire repeating unit cell (e.g., Fig. 6(e)). This distribution enables in the present problems the monitoring of the strain-energy function ψ and its growth at each location to its critical value. The first location at which the critical value is reached indicates the loss of static stability and failure initiation.

Generalizations of the present methodology to the analysis of composite plate and shells that are composed of softening hyperelastic materials reinforced in various orientations are possible. In such generalizations, the micromechanically established macroscopic constitutive equations are applied at every integration point of a finite element analysis.

Biological tissues form multiphase composites which are composed of various types of hyperelastic constituents. The arterial wall, for example, consists of intima, media, and adventitia layers which can be modeled as distinct hyperelastic materials, for example, see Gasser et al. [24]. Standard hyperelastic energy functions have been incorporated with the finite strain HFGMC method and then coupled to a finite element solver by Kim [25] and Kim et al. [26] to investigate the behavior of various tissue materials including the human arterial wall layers and porcine aortic valves leaflets. Such an investigation can be extended to incorporate hyperelastic energy functions with limiters to be applied for the establishment of the macroscopic constitutive equations and for the prediction of failure initiation in this type of composite materials. In the case of monolithic (unreinforced) biological materials, failure prediction has been implemented by Volokh [7] and Balakhovsky et al. [27].

Acknowledgment

The first author was grateful for the support of the German-Israel Foundation (GIF) under Contract No. 1166-163.

References

- [1] Christensen, R. M., 2013, *The Theory of Materials Failure*, Oxford University Press, Oxford, UK.
- [2] Gosse, J. H., and Christensen, R. M., 2001, "Strain Invariant Failure Criteria for Polymers in Composite Materials," *AIAA Paper No.* 2001-1184.
- [3] Humphrey, J. D., 2002, *Cardiovascular Solid Mechanics*, Springer, New York.
- [4] Aboudi, J., Arnold, S. M., and Bednarczyk, B. A., 2013, *Micromechanics of Composite Materials: A Generalized Multiscale Analysis Approach*, Elsevier, Oxford, UK.
- [5] Volokh, K. Y., 2013, "Review of the Energy Limiters Approach to Modeling Failure of Rubber," *Rubber Chem. Technol.*, **86**(3), pp. 470–487.
- [6] Volokh, K. Y., 2010, "On Modeling Failure of Rubber-Like Materials," *Mech. Res. Commun.*, **37**(8), pp. 684–689.
- [7] Volokh, K. Y., 2010, "Comparison of Biomechanical Failure Criteria for Abdominal Aortic Aneurysm," *J. Biomech.*, **43**(10), pp. 2032–2034.
- [8] Aboudi, J., and Pindera, M.-J., 2004, "High-Fidelity Micromechanical Modeling of Continuously Reinforced Elastic Multiphase Materials Undergoing Finite Deformation," *Math. Mech. Solids*, **9**(6), pp. 599–628.
- [9] Aboudi, J., 2009, "Finite Strain Micromechanical Analysis of Rubber-Like Matrix Composites Incorporating the Mullins Damage Effect," *Int. J. Damage Mech.*, **18**(1), pp. 5–29.
- [10] Ogden, R. W., 1984, *Non-Linear Elastic Deformations*, Ellis Horwood, Chichester, UK.
- [11] Holzapfel, G. A., 2000, *Nonlinear Solid Mechanics*, Wiley, New York.
- [12] Volokh, K. Y., 2014, "On Irreversibility and Dissipation in Hyperelasticity With Softening," *ASME J. Appl. Mech.*, **81**(7), p. 074501.
- [13] Wang, J., Duan, H. L., Zhang, Z., and Huang, Z. P., 2005, "An Anti-Interpenetration Model and Connections Between Interphase and Interface Models in Particle-Reinforced Composites," *Int. J. Mech. Sci.*, **47**(4–5), pp. 701–718.
- [14] Jafari, A. H., Abeyaratne, R., and Horgan, C. O., 1984, "The Finite Deformation of a Pressurized Circular Tube for a Class of Compressible Materials," *J. Appl. Math. Phys. (ZAMP)*, **35**(2), pp. 227–246.
- [15] Houghton, D. M., 1987, "Inflation and Bifurcation of Thick-Walled Compressible Elastic Spherical Shells," *IMA J. Appl. Math.*, **39**(3), pp. 259–272.
- [16] Blatz, P. J., and Ko, W. L., 1962, "Application of Finite Elastic Theory to the Deformation of Rubbery Materials," *Trans. Soc. Rheol.*, **6**(1), pp. 223–251.
- [17] Horgan, C. O., 1995, "On Axisymmetric Solutions for Compressible Nonlinearly Elastic Solids," *J. Appl. Math. Phys. (ZAMP)*, **46**, pp. S107–S125.
- [18] Horgan, C. O., 2001, "Equilibrium Solutions for Compressible Nonlinearly Elastic Material," *Nonlinear Elasticity: Theory and Applications*, R. W. Ogden and Y. Fu, eds., Cambridge University Press, Cambridge, UK, pp. 135–159.
- [19] Hashin, Z., and Rosen, B. W., 1964, "The Elastic Moduli of Fiber-Reinforced Materials," *ASME J. Appl. Mech.*, **31**(2), pp. 223–232.
- [20] Chung, D. T., Horgan, C. O., and Abeyaratne, R., 1986, "The Finite Deformation of Internally Pressurized Hollow Cylinders and Spheres for a Class of Compressible Elastic Materials," *Int. J. Solids Struct.*, **22**(12), pp. 1557–1570.
- [21] Hamdi, A., Nait Abdelaziz, M., Ait Hocine, N., Heuillet, P., and Benseddiq, N., 2006, "A Fracture Criterion of Rubber-Like Materials Under Plane Stress Conditions," *Polym. Test.*, **25**(8), pp. 994–1005.
- [22] Yeoh, O. H., 1990, "Characterization of Elastic Properties of Carbon Black Filled Rubber Vulcanizates," *Rubber Chem. Technol.*, **63**(5), pp. 792–805.
- [23] Assaad, M., and Arnold, S. M., 1999, "An Analysis of the Macroscopic Tensile Behavior of a Nonlinear Nylon Reinforced Elastomeric Composite System Using MAC/GMC," NASA Glenn Research Center, Cleveland, OH, Paper No. NASA/TM-1999-209066.
- [24] Gasser, T. C., Ogden, R. W., and Holzapfel, G. A., 2006, "Hyperelastic Modeling of Arterial Layers With Distributed Collagen Fibre Orientations," *J. R. Soc. Interface*, **3**(6), pp. 15–35.
- [25] Kim, H. S., 2009, "Nonlinear Multiscale Anisotropic Material and Structural Models for Prosthetic and Native Aortic Heart Valves," Ph.D. dissertation, Georgia Institute of Technology, Atlanta, GA.
- [26] Kim, H. S., Haj-Ali, R., and Aboudi, J., 2010, "Nonlinear Micromechanical Modeling Approach for Anisotropic Hyperelastic Tissue Materials," 1st International Conference on Advances in Interaction and Multiscale Mechanics, Jeju, South Korea, May 31–June 2.
- [27] Balakhovskiy, K., Jabareen, M., and Volokh, K., 2014, "Modeling Rupture of Growing Aneurysms," *J. Biomech.*, **47**(3), pp. 653–658.